Applied Clay Science 160 (2018) 249–262

Contents lists available at ScienceDirect

Applied Clay Science

journal homepage: www.elsevier.com/locate/clay

Research paper

Hyperspectral remote sensing for mapping and detection of Egyptian kaolin quality

Mahmoud E. Awad[a,c,d,*], Reda Amer[b], Alberto López-Galindo[c], Mahmoud M. El-Rahmany[a], Luis F. García del Moral[e], César Viseras[c,d]

[a] Department of Geology, Faculty of Science, Al Azhar University in Cairo, 11884, Egypt
[b] Department of Earth and Environmental Sciences, Tulane University, USA
[c] Instituto Andaluz de Ciencias de la Tierra (IACT), CSIC-Universidad de Granada, Spain
[d] Departamento de Farmacia y Tecnología Farmacéutica, Universidad de Granada, Spain
[e] Departamento de Fisiología Vegetal, Universidad de Granada, Spain

ARTICLE INFO

Keywords:
Egypt
Abu Zenima
Kaolin
Hyperspectral parameters
Hyperion image
Structural order-disorder

ABSTRACT

This study aims to use spectral analysis and hyperspectral Hyperion remote sensing images of the Egyptian Abu Zenima Carboniferous and Cretaceous kaolin deposits, located in West-Central Sinai Peninsula, for mapping the spatial distribution of their qualities determined by their mineralogical and geochemical parameters. Mineral quantification has been made by X-ray diffractometry and chemical analysis, and kaolinite structural order-disorder degree was measured by mean of the Hinckley (HI), Stoch (IK) and Liètard (R2) indices. The geochemical characteristics classified the studied samples into ferruginous and non-ferruginous deposits. The mineralogical composition discriminated the studied sample grades into kaolin (> 75% kaolinite), silty kaolin (75–50% kaolinite) and kaolinitic siltstone (< 50% kaolinite). Abu Zenima kaolin quality is mainly influenced by quartz and Fe-Ti minerals contents. The Carboniferous kaolin samples are characterized by ordered kaolinite (HI or R2 > 1 and IK < 0.7), while the Cretaceous kaolins exhibited mainly disordered kaolinite (HI or R2 < 1 and IK > 0.7). Five EO-1 Hyperion Level 1 GST radiometrically and geometrically corrected images of April and May 2011 were used to identify the spatial distribution of Carboniferous and Cretaceous kaolin grades and the structural characteristics of kaolinite. The position, depth, full-width-half-maximum and 22SP-Index of the absorption features were calculated for the continuum-removed spectra in the range 350–2500 nm. Prominent absorption features spectra occur around ~1400, ~1900, ~2200 and 2300 nm, and there are shifting and changes in their position and morphology with the kaolinite richness and the structural order-disorder degree. Spectral Angle Mapper (SAM) supervised classifications proved successfulness for identifying the kaolinite spatial distribution on the Hyperion images using the measured spectra of kaolins with different qualities and structural order-disorders.

1. Introduction

Kaolin is a fine usually white clay mainly made up of the clay mineral kaolinite and/or halloysite (> 75%; Kogel et al., 2006). It is a naturally abundant and inexpensive geomaterial and exhibits many various suitable properties that make it useful in numerous industrial, agricultural, civil, environmental and health-care applications (Ciullo, 1996; Murray, 1999; Carretero et al., 2013; Awad et al., 2017b). The remarkable kaolin resources are mined worldwide form giant districts located in the United States (the upper coastal plain areas of Georgia and south Carolina), Brazil (eastern Amazon region), the United Kingdom (Cornwall–Devon) and Germany (Bavaria and Saxony). However, numerous other significant kaolin occurrences, either exploited or not, are recorded in many countries of the world's continents except of Antarctica (Kogel et al., 2006).

According to the global statistical Mundi Index (2007), Egypt is the first kaolin producer in Africa and the Middle East, with the rank 19th worldwide (Ekosse, 2010). The total production of Egyptian kaolins in the last decade is about 3,702,000 metric tons, with an average of 375,000 metric tons per year, representing 1% of the worldwide production (Taib, 2015; Virta, 2015). Based on supply and demand of the local market of industrial minerals in Egypt, these deposits are essentially exploited, since the mid of the 20th century, as raw materials for ceramics, refractories, Portland cement, fillers, paints and paper

* Corresponding author at: Department of Geology, Faculty of Science, Al Azhar University in Cairo, 11884, Egypt.
E-mail address: mawad@azhar.edu.eg (M.E. Awad).

https://doi.org/10.1016/j.clay.2018.02.042
Received 26 September 2017; Received in revised form 8 February 2018; Accepted 27 February 2018
Available online 06 March 2018
0169-1317/

industries (Abdel Shafy, 1967; Hegab et al., 1992; Rashed and Amer, 1994; Kamel et al., 1997). Awad et al. (2017a) have recently characterized some of the Egyptian kaolins, evaluating their mineralogical and chemical composition, purity, crystallinity, color, and rheology, trying to find alternative applications in health-care uses (i.e., pharmaceutical and cosmetic applications).

The grade and quality of economic kaolin deposits, as a raw material for industrial uses, are mainly determined on the basis of the kaolinite content and its structural order-disorder degree, as well as the associated quartz and Fe-Ti mineral impurities as mainly host of heavy metals (Vie et al., 2007; Teh et al., 2009; Gupta et al., 2011; Ptáček et al., 2013; Wardhana et al., 2014; Ndlovu et al., 2015).

Kaolin chemistry and mineralogy are normally affected by its genesis, from the source rock weathering, sediment transport till the depositional and diagenetic conditions, which have a strong influence on its physical properties such as color, opacity and whiteness, compactness, plasticity, and rheology, or its physicochemical properties, including sorption or cationic exchange capacities (Murray and Lyons, 1955, 1959; Vasilev et al., 1976; Cabrera and Eddleston, 1983; LaIglesia and Aznar, 1996; Fialips et al., 2000; Awad et al., 2017a).

The kaolinite structural order-disorder (i.e., the perfection degree of the phyllosilicate layers stacking) was calculated by first time by Hinckley (1963) who proposed an index (HI) that is considered as the most common. Beyond the HI, other six structural order indices were also introduced, including the QF index (Range and Weiss, 1969), the IK index (Stoch, 1974), the R2 index (Liétard, 1977), the H&B index (Hughes and Brown, 1979), the expert system (Plançon and Zacharie, 1990) and FWHM indices (Amigo et al., 1994).

The color spectrophotometric analysis (wavelength range from 400 to 700 nm) proved to be a helpful tool for discriminating mineralogical quality of kaolins, as strong relationships exist between the iron oxide contents and the CIE-lab chromatic and lightness parameters (Awad et al., 2017a). On the other hand, kaolinite and most of the mineral surfaces show diagnostic spectral signatures in Visible/Near Infrared (VNIR) and Shortwave Infrared (SWIR) of electromagnetic spectrum, which enables their detection (Hunt, 1977; Clark et al., 1990; Rowan et al., 2003; Kruse et al., 2006). Absorption features at specific wavelengths result from both, electronic and vibrational processes in molecules (Hunt and Salisbury, 1970, 1971), and they are caused by electronic processes that generally occur at wavelengths $< 1\,\mu m$ (VNIR spectrum), whereas the vibrational process occurs at wavelengths $> 0.94\,\mu m$ (SWIR spectrum, Hunt, 1977). Mineral absorption features are usually generated by the overtone or the combination of fundamental and overtone transitions of the vibrations of atom bonds. Absorption features at ~1400 nm and 2200 to 2400 nm are used in the identification of hydroxylated minerals, while minerals with absorption features at ~1910 nm and 2200 to 2400 nm are likely hydrated minerals. Minerals with three absorption features at ~1400 nm, ~1910 nm and 2200 to 2400 nm are usually identified as hydrated phyllosilicates (Poulet et al., 2005; Mustard et al., 2008). For example, clay minerals (like kaolinite, illite, and montmorillonite) have an absorption peak around 2206 nm, corresponding to the combination of(OH) stretch and Al-OH bending modes (Goetz, 1992; Kruse et al., 1993), and carbonate minerals (e.g. calcite) has an absorption peak around 2348 nm corresponding to CO_3 overtone vibrations (Gaffey, 1986). Spectral analysis of clay minerals indicated that their absorption features shift due to variations in composition and crystal structure (Kruse and Hauff, 1991; Hauff, 1991). Zhang et al. (2001) reported that the SWIR reflectance spectroscopy is capable of detecting clay minerals at abundances as low as 1 wt% and quantitatively estimating the structural order-disorder of kaolinite by defining a "14Sp Index" (calculated as A-B/A), where A and B correspond to the depths of the absorption feature doubled found around 1400 nm on the kaolinite spectra. Hyperspectral sensors acquire simultaneously images of the Earth surface in tens to hundreds of narrow spectral bands in such a way that a complete spectral pattern of each pixel can be derived for target detection, discrimination and classification (Kerekes and Baum, 2003).

Remote sensing techniques have been widely and successfully used for geological mapping and mineral exploration for decades (Goetz and Strivastava, 1985; Sultan et al., 1986; Boardman and Kruse, 1994; Rowan and Mars, 2003; Perry, 2004; Zhang et al., 2007; Amer et al., 2010; Amer et al., 2012a, 2012b, 2015; Pour and Hashim, 2011, 2012). The Hyperion hyperspectral images were used for several surface mineral mapping with significant accuracy (Jafari and Lewis, 2012; Kusuma et al., 2012; Farifteh et al., 2013).

With these premises and for an optimum valorization, it could be an interesting objective to functionalize the mineralogical and geochemical aspects integrated with hyperspectral parameters for discriminating grades of kaolin deposits (kaolinite richness and structural order-disorder), on regional scale occurrences, by means of the reconnaissance satellite imageries. Hence, the aim of this study is to use the measurements of VNIR and SWIR reflectance and Hyperion imagery with mineralogical and geochemical data to evaluate the usefulness of remote sensing techniques in mapping and detecting the kaolin purity and kaolinite structural order of the Egyptian Abu Zenima kaolin deposits. The proposed methodologies were applied on six lithological sections, located at Abu Zenima district, and related to different geologic formations and ages. The results could be also used as local and regional model for prospecting the high purity kaolin zones in the outcropped relevant bearing rock units.

2. Study site and geologic setting

Abu Zenima sedimentary kaolin resource, located between longitude 33° 14′ 00″ and 33° 24′ 00″ E and latitude 28° 52′ 00″ and 29° 10′ 00″ N at West-Central Sinai Peninsula, is one of the greatest reserve of economic interest in Egypt. It represents the highest quality amongst all the Egyptian kaolins and recorded by 120 million tons (Abd El Razek, 1994). The sedimentary basin of Abu Zenima district covers about 333 km^2 of cultivated and accessible lands, generally elevated up to 680–1000 m above sea level. The major outcrops of kaolin-bearing rocks at Abu Zenima district are exposed at Wadi Khaboba (K) and Gabal Hazbar (H) areas, located to the northern part of Abu Zenima district, and Wadi Abu Natash (N), Farsh El Ghozlan (F), Wadi Budra (B) and Gabal El Dehessa (D) sites, located to the South (Fig. 1).

The stratigraphic succession of the studied Abu Zenima district is ranged from the basement Pre-Cambrian rocks till the Quaternary deposits. The Pre-Cambrian basement rocks are considered as probable sources of the studied sedimentary kaolin deposits (Baioumy et al., 2012; Baioumy, 2014a, 2014b). These are mainly included by metamorphic schists, gneisses and migmatites, dark amphibolitic xenoliths of dioritic to quartz dioritic rocks and old granitoids intruded by younger pink granites and variable composition sets of dykes. The sediments were intruded by Triassic dolerite sills scattered in the central and southern portions of the area. The successions at the northern region were generally extruded by Miocene basaltic dykes with a main trend NE-SW direction (El Aref et al., 1988; Abdel Karim, 1996). The kaolin-bearing member at the studied Wadi Khaboba, Gabal Hazbar and Wadi Abu Natash sections is related to the Abu Thora Formation, with a the Lower Carboniferous (Visean) age (Kora, 1989, 1995). The kaolin-bearing member exposed at Gabal El Dehessa, Farsh El Ghozlan and Wadi Budra belongs to the Malha Formation, with a the Lower Cretaceous (Albian) age (Abdallah et al., 1963; Saied, 1990). Fig. 2 summarizes the lithology of the studied sections and location of studied samples. Lithology was described in detail in Awad et al. (2017a).

3. Materials and methods

Twenty-nine rock samples were collected from the Carboniferous outcrops, and thirty-six samples were collected from the Lower Cretaceous ones. The methods used for chemical composition, mineral identification and quantification were explained in Awad et al. (2017a).

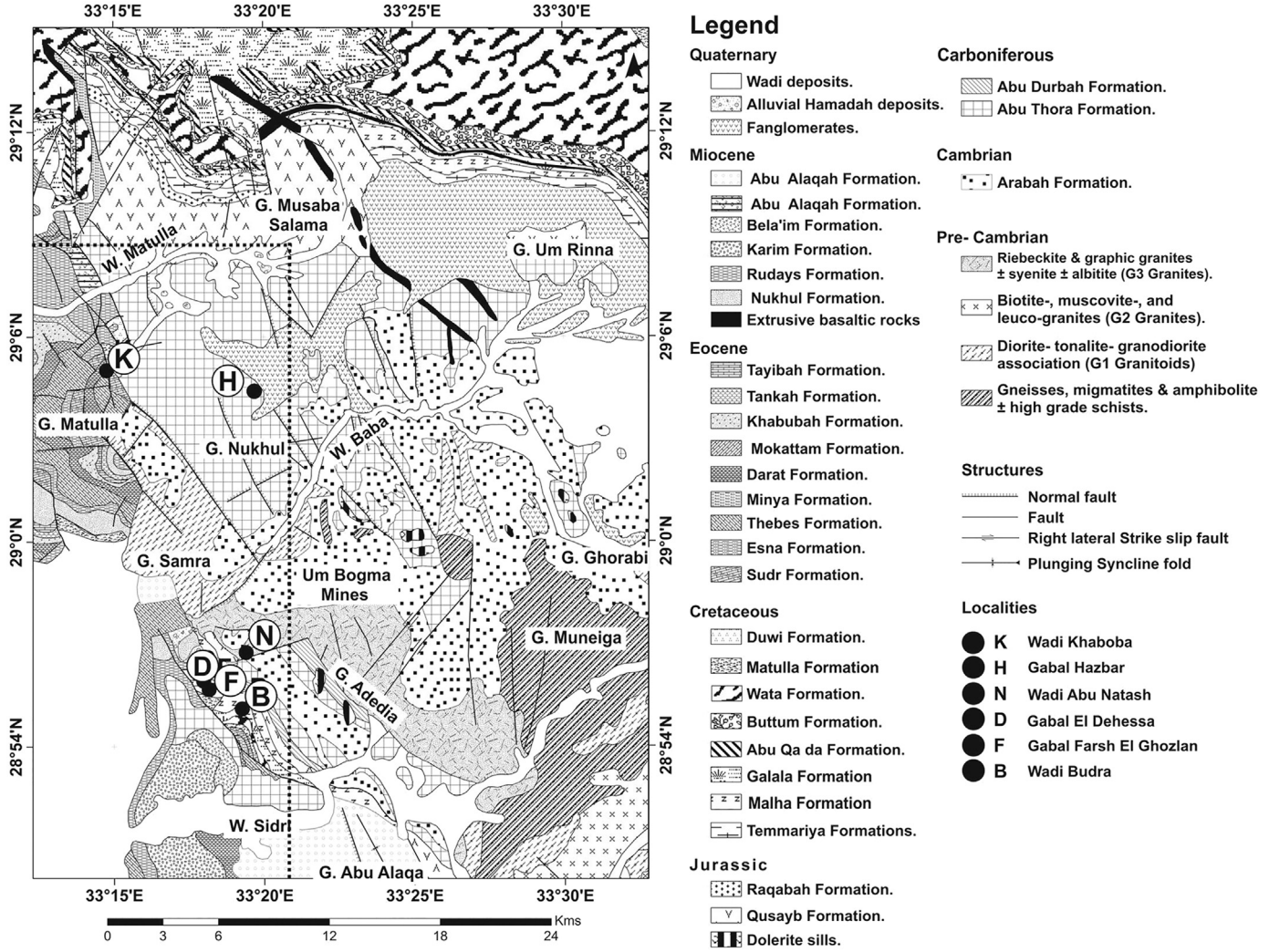

Fig. 1. Geological map of the study area (modified from Conoco, 1987).

The Al_2O_3/SiO_2 and $Log(Fe_2O_3/K_2O)$ vs $Log\ (SiO_2/Al_2O_3)$ ratios was used to discriminate the kaolin grades (Kogel et al., 2006) and iron content variabilities (Herron, 1988).

The spectral analyses were performed to the raw samples with > 50% kaolinite, for two modules, consolidated and powdered samples, by using an Analytical Spectrometer Device (ASD) Portable Spectroradiometer FieldSpec Pro JR (A109200), with spectral ranges 350–2500 nm. The spectral resolutions are 3 nm at 700 nm, and 30 nm at 1400 and 2100 nm, with a total number of 2151 spectral bands. The measuring interval was 1.4 nm for the spectral range 350–1000 nm and 2 nm for the range 1000–2500 nm. The system is incorporated by a contact probean high intensity contact probe A122307 with halogenous light source and measurement surface area equivalent to a circle 2 cm in diameter, and a maximum specular reflectance of 5%. White level was calibrated on a Spectralon of 3.62″ diameter (Analytical Spectral Devices Inc.), material with approximately 100% reflectance across the entire spectrum.

Spectra were visualized by SigmaPlot-13® and ENVI 5.4 software. The continuum spectral data was calculated by using the Origin® software, on the basis of mathematical polynomial fitting approach of the spectral curve (at equation order = 9 and total number of coordinal points (λ,R_0) equals 2151) to obtain new y-coordinate data of the reflectance (R_C) corresponding to the wavelength values in the range (350–2500) of each spectral curve (λ, R_C). The continuum was then removed from the reflectance data according to the method of Clark and Roush (1984) by dividing the initial reflectance (R_0) data by the values (R_C) obtained from the curve fitting to get the new continuum-removed data. The continuum-removed ratio data were plotted against the corresponding wavelength values using again SigmaPlot® software to obtain new normalized curves at the baseline (y = 1). Then, the spectral parameters were determined by fit multi-peak analysis using Origin® software. Continuum-removal normalizes the reflectance spectra from a common baseline. The position attribute is the wavelength of the lowest point, the depth is the reflectance of the low point, and FWHM is the width of the feature at half of the depth (Kruse et al., 1993). Because the absence of the 1400 nm doublets on all the spectral curves, a 22SP-Index was calculated for the 2200 nm doublet absorption feature using a similar relationship (A − B)/A to that introduced by Zhang et al. (2001) (Fig. 3).

The kaolinite structural order-disorder degree was determined by three indices: (1) the Hinckley index (HI, Hinckley, 1963) was determined by using the reflections (02*l*) and(11*l*) in the range from 19° to 26° 2θ in random oriented powdered samples, as they are very sensitive to the structural defects (i.e., random and interlayer displacements) in kaolinite structure; it was calculated as the ratio of summation (1 − 10) and (11 − 1) reflection heights above their background from 20° to 22° 2θ to the (1–10) reflection height above the total background from 19° to 26°2θ; (2) the Stoch index (IK, Stoch, 1974) was measured in the same 2θ range of the HI as the ratio of the (020) to the (1–10) reflection heights above the background from 19° to 24° 2θ; and (3) the Liétard index (R2, Liétard, 1977), was calculated by heights of the (1 − 31) and the (131) reflections and the height of the valley between them, all

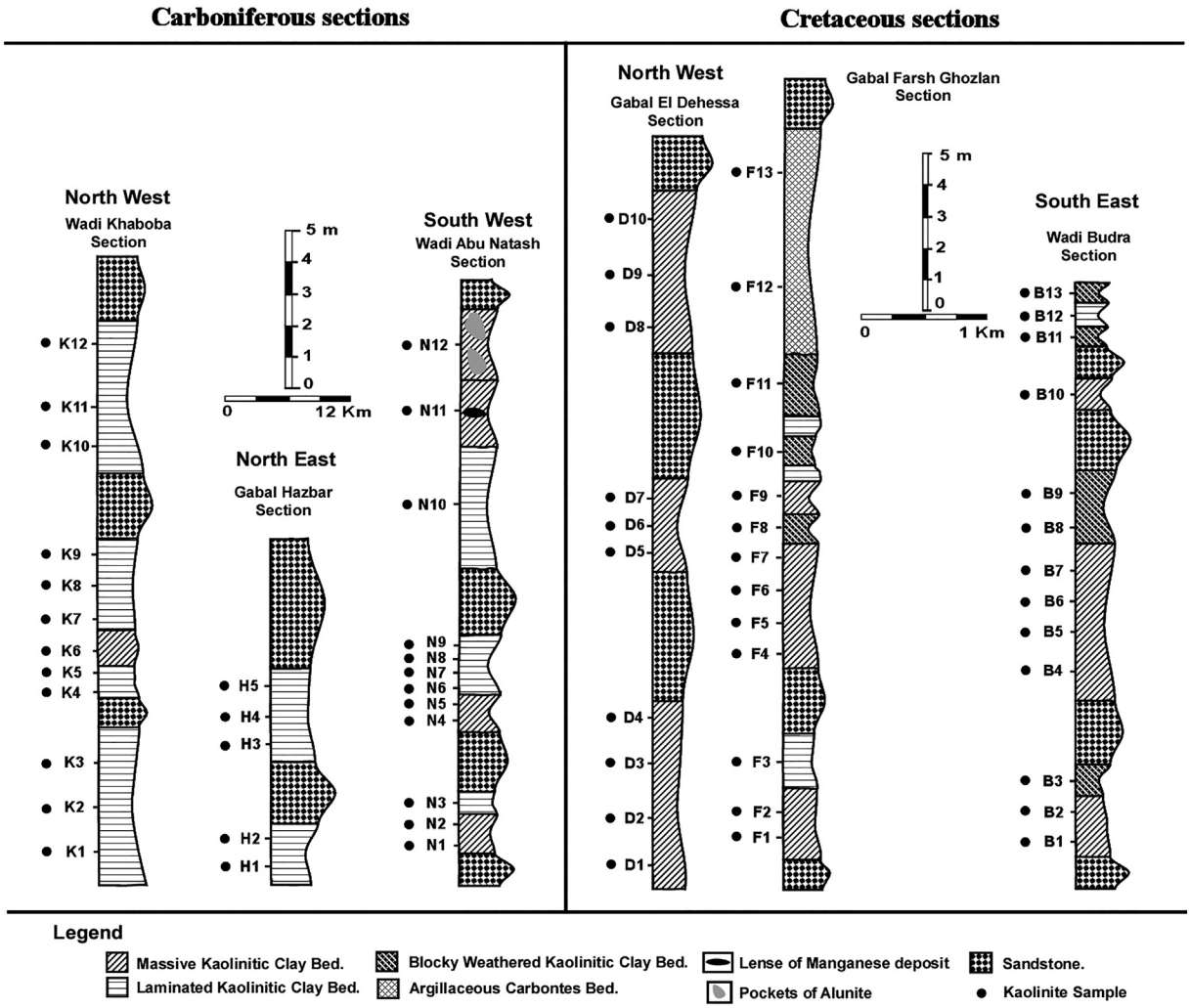

Fig. 2. Lithology and sampling of the Carboniferous and Cretaceous sedimentary kaolin deposits, from North to South, of the Abu Zenima district, Sinai Peninsula.

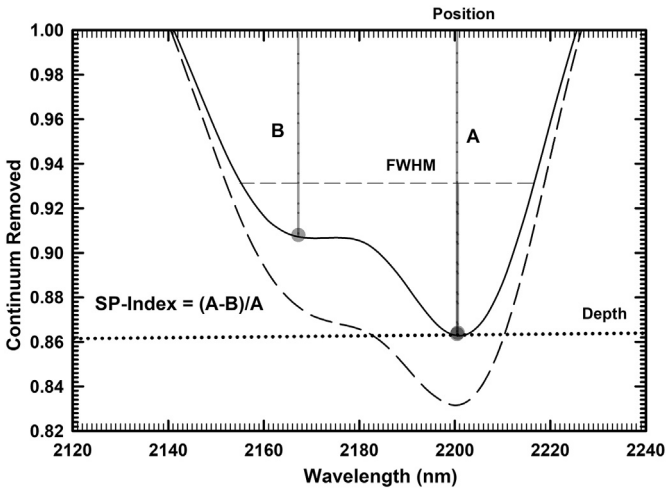

Fig. 3. Calculation procedure method for the spectral measured parameters: position, depth, FWHM and 22SP-index.

measured above the background between 37° and 40° 2θ. The confidence of using the HI, R2 and IK, amongst all other indices, for detecting the spatial distribution of the studied kaolinite order-disorder degree, is based on their influence by the mineral impurities. Hence, such indices values calculated for high grade kaolin samples are more objective (Aparicio and Galán, 1999).

Five EO-1 Hyperion Level 1 GST radiometrically and geometrically corrected images of April and May 2011 were used to study the spatial distribution of kaolinite in Abu Zenima area. The image consists of 242 spectral channels in the wavelength ranges 400–2500 nm of the electromagnetic spectrum, with a spectral and spatial resolution of 10 nm and 30 m, respectively. The Hyperion visible-near-infrared (VNIR) sensor has 70 bands (1–70), and the shortwave-infrared (SWIR) sensor has 172 bands (71–242). Hyperion image has some bad bands which include bands 1–7, 58–76, and 225–242 which already set to values of zero (Barry, 2001). Bands 121–126, 167–180 and 222–224 have severe noise that corresponds to strong water vapor absorption, and are typically removed from processing (Datt et al., 2003). Hyperion image consists of 175 bands after removing all of the bad bands. The five images were radiometrically calibrated for retrieving spectral reflectance using ENVI 5.4 automated module FLAASH and mosaicked into one image. Image processing and analysis were carried out using ENVI 5.5 and ArcGIS 10.5 software packages. Spectral Angle Mapper (SAM) algorithm was used to identify the spatial distribution of the kaolinite using the measured spectra. SAM is a deterministic method that looks for an exact pixel match by measuring the spectral similarity between the pixel and reference spectra by calculating the angle between the two spectra, treating them as vectors in *n*-dimensional space, the smaller the angle the more likely the spectra are similar (Kruse et al., 1993).

Table 1
Selected mineralogical, chemical, SWIR hyperspectral parameters and structural order indices of the studied kaolin samples.

Period	Sections	Samples	Mineralogy					Chemical parameters				Spectral parameters							Structural order		
			Kaolinite %	Quartz %	Fe-Ti Min. %	K-Si[a] Min. %	Other minerals %	Al_2O_3/SiO_2	Log (Fe_2O_3/K_2O)	TiO_2 wt%	Fe_2O_3 wt%	Position 1400 nm	Depth 1400 nm	FWHM 1400 nm	Position 2200 nm	Depth 2200 nm	FWHM 2200 nm	SP-Index 2200 nm	HI	IK	R2
Carboniferous	Wadi Khaboba (K)	K1	88	7	1	3	1	0.74	0.01	1.33	0.53	1402	0.844	43.86	2200	0.858	56.35	0.312	1.28	0.64	1.16
		K2	84	1	10	5	–	0.83	1.23	1.15	8.91	1402	0.874	43.39	2201	0.855	56.16	0.301	1.30	0.74	1.10
		K3	89	5	1	4	1	0.77	0.03	1.3	0.52	1402	0.856	46.19	2201	0.856	54.41	0.288	1.33	0.67	1.13
		K4	65	23	1	4	7	0.53	−0.31	1.59	0.58	1403	0.928	37.82	2202	0.876	53.54	0.301	–	–	–
		K5	80	13	3	4	–	0.62	0.17	1.83	1.11	1402	0.885	43.57	2201	0.835	56.33	0.316	1.38	0.72	1.20
		K6	65	24	2	5	4	0.52	0.04	1.53	1.17	1403	0.926	37.65	2202	0.877	54.33	0.383	–	–	–
		K7	64	26	2	7	1	0.48	−0.07	1.61	0.8	1403	0.924	39.93	2202	0.883	50.12	0.396	–	–	–
		K8	63	24	1	6	6	0.51	−0.28	1.55	0.63	1404	0.931	38.14	2202	0.889	51.38	0.368	–	–	–
		K9	67	22	2	7	2	0.51	−0.12	1.92	0.66	1403	0.921	37.16	2202	0.876	52.36	0.386	–	–	–
		K10	57	28	2	13	–	0.39	−0.35	1.81	0.61	1404	0.965	36.16	2203	0.899	47.24	0.457	–	–	–
		K11	40	48	2	5	5	0.27	−0.49	1.78	0.41	–	–	–	–	–	–	–	–	–	–
		K12	72	17	5	6	–	0.56	0.71	1.73	3.43	1403	0.911	41.65	2201	0.87	53.74	0.363	–	–	–
	Gabal Hazbar (H)	H1	55	36	1	8	–	0.37	−0.15	1.33	0.49	–	–	–	–	–	–	–	–	–	–
		H2	58	32	2	8	–	0.42	0.17	1.41	1.06	1404	0.94	37.98	2202	0.896	47.83	0.419	–	–	–
		H3	43	48	1	8	–	0.27	−0.1	1.57	0.64	–	–	–	–	–	–	–	–	–	–
		H4	57	31	1	3	8	0.21	−0.44	1.23	0.37	1404	0.971	37.16	2202	0.934	46.26	0.457	–	–	–
		H5	81	14	2	3	–	0.61	0.07	1.79	0.6	1403	0.894	42.2	2200	0.849	56.16	0.32	1.33	0.76	1.11
	Wadi Abu Natash (N)	N1	93	–	5	–	2	0.89	2.25	3.29	1.76	1401	0.747	46.45	2200	0.802	61.67	0.307	1.46	0.54	1.20
		N2	96	–	3	–	1	0.87	1.61	3.36	0.81	1401	0.752	48.84	2200	0.794	64.04	0.298	1.50	0.54	1.18
		N3	93	–	4	–	3	0.88	1.62	3.42	0.84	1402	0.764	47.47	2201	0.797	63.05	0.306	1.42	0.62	1.20
		N4	95	–	4	–	1	0.88	1.53	3.32	1.01	1401	0.823	45.12	2200	0.81	62.66	0.326	1.48	0.55	1.17
		N5	92	–	7	–	1	0.89	1.7	3.57	3	1402	0.868	44.55	2200	0.824	58.07	0.348	1.46	0.61	1.20
		N6	94	–	4	–	2	0.9	0.78	3.15	0.6	1401	0.783	46.34	2200	0.813	62.07	0.341	1.39	0.57	1.20
		N7	69	22	2	5	2	0.46	0.5	1.47	1.46	1403	0.939	40.57	2202	0.896	50	0.446	–	–	–
		N8	68	25	4	3	–	0.41	0.85	1.48	2.83	1404	0.936	42.22	2201	0.906	47.33	0.423	–	–	–
		N9	69	23	3	5	–	0.51	0.33	1.91	1.18	1403	0.941	38.65	2202	0.892	51.24	0.401	–	–	–
		N10	17	20	21	42	–	0.36	0.68	0.89	21.34	–	–	–	–	–	–	–	–	–	–
		N11	87	–	4	–	9	0.89	1.5	3.29	0.95	1402	0.764	48.57	2200	0.842	55.44	0.292	1.50	0.56	1.20
		N12	92	1	2	–	5	0.92	0.29	0.19	1.97	1402	0.822	49.23	2201	0.787	57.87	0.301	1.29	0.60	1.02

(*continued on next page*)

Table 1 (*continued*)

Period	Sections	Samples	Mineralogy					Chemical parameters				Spectral parameters							Structural order		
			Kaolinite %	Quartz %	Fe-Ti Min. %	K-Si[a] Min. %	Other minerals %	Al_2O_3/SiO_2	Log (Fe_2O_3/K_2O)	TiO_2 wt%	Fe_2O_3 wt%	Position 1400 nm	Depth 1400 nm	FWHM 1400 nm	Position 2200 nm	Depth 2200 nm	FWHM 2200 nm	SP-Index 2200 nm	HI	IK	R2
Cretaceous	Gabal El Dehessa (D)	D1	78	18	3	–	1	0.57	1.16	2.31	1.31	1402	0.864	47.79	2200	0.83	56.53	0.252	0.54	1.23	0.72
		D2	77	20	3	–	–	0.55	1.54	2.74	1.03	1403	0.868	48.14	2201	0.823	55.67	0.271	0.55	0.99	0.72
		D3	79	18	3	–	–	0.57	1.72	2.57	1.56	1402	0.838	49.19	2201	0.826	57.83	0.263	0.50	1.22	0.52
		D4	71	24	5	–	–	0.49	1.78	2.7	1.81	1402	0.875	44.26	2201	0.846	55.19	0.343	–	–	–
		D5	83	14	3	–	–	0.62	0.97	2.48	0.94	1403	0.849	46.62	2200	0.832	57.15	0.273	0.82	1.19	0.78
		D6	93	3	4	–	–	0.85	1.53	3.13	1.36	1401	0.833	51.51	2200	0.799	59.54	0.234	0.27	1.29	0.48
		D7	92	3	4	1	–	0.84	1.65	3.51	1.78	1401	0.79	52.39	2200	0.797	62.3	0.231	0.47	1.29	0.53
		D8	77	20	3	–	–	0.52	1	2.28	0.9	1403	0.856	46.07	2201	0.826	57.32	0.281	0.80	0.97	0.83
		D9	93	4	3	–	–	0.79	1.45	2.78	0.85	1401	0.792	50.45	2200	0.807	61.45	0.254	0.63	1.17	0.77
		D10	78	18	4	–	–	0.57	1.08	3.22	0.97	1403	0.858	44.77	2201	0.831	58.62	0.286	0.82	1.09	0.78
	Farsh El Ghozlan (F)	F1	89	9	2	–	–	0.7	1.68	2.5	0.96	1402	0.813	49.64	2200	0.837	62.92	0.241	0.53	1.22	0.61
		F2	95	2	3	–	–	0.86	1.64	2.87	0.87	1401	0.824	50.86	2200	0.797	58.63	0.221	0.45	1.50	0.48
		F3	94	3	3	–	–	0.79	1.7	2.33	1.52	1402	0.781	52.88	2200	0.797	60.89	0.251	0.59	1.03	0.59
		F4	79	17	4	–	–	0.58	1.2	2.23	2.05	1402	0.856	46.42	2201	0.832	57.47	0.271	0.68	1.14	0.64
		F5	84	12	4	–	–	0.66	1.58	2.28	2.27	1402	0.855	50.45	2201	0.831	60.69	0.255	0.52	1.13	0.55
		F6	67	28	4	–	1	0.45	1.29	3.42	0.97	1403	0.882	43.68	2202	0.843	55.33	0.397	–	–	–
		F7	78	18	4	–	–	0.57	1.45	2.54	1.98	1403	0.904	41.03	2201	0.855	53.42	0.272	0.66	1.09	0.68
		F8	88	7	4	1	–	0.76	1.39	2.42	2.43	1402	0.856	47.6	2201	0.843	56.89	0.243	0.72	1.16	0.64
		F9	85	11	4	–	–	0.66	1.38	3.55	0.95	1402	0.832	48.82	2200	0.835	61.48	0.254	0.61	1.03	0.61
		F10	78	13	6	2	1	0.63	1.26	1.82	4.75	1402	0.939	42.74	2201	0.873	52.22	0.292	0.95	1.02	0.88
		F11	55	21	6	16	2	0.41	0.33	1.09	5.74	1405	0.957	41.27	2203	0.937	45.17	0.519	–	–	–
		F12	24	17	5	20	34	0.45	0.29	0.9	4.68	–	–	–	–	–	–	–	–	–	–
		F13	9	4	2	–	85	0.42	0.63	0.2	2.3	–	–	–	–	–	–	–	–	–	–
	Wadi Budra (B)	B1	65	18	12	3	2	0.52	1.72	1.65	10.45	1404	0.849	45.77	2201	0.861	52.36	0.275	–	–	–
		B2	60	21	12	5	2	0.46	1.29	2.07	9.74	1404	0.962	42.15	2202	0.93	46.62	0.48	–	–	–
		B3	86	3	7	–	4	0.77	1.85	1.62	5	1402	0.916	48.41	2200	0.868	53.56	0.281	0.99	0.89	0.94
		B4	67	20	7	3	3	0.54	1.13	2.35	5.21	1405	0.952	43.36	2202	0.909	46.65	0.416	–	–	–
		B5	65	13	19	–	3	0.69	1.86	1.98	16.71	1404	0.969	41.89	2201	0.923	49.83	0.422	–	–	–
		B6	53	15	5	–	27	0.51	0.19	1.5	4.01	1405	0.928	42.28	2203	0.942	44.78	0.401	–	–	–
		B7	22	–	5	26	47	0.47	−0.1	1.72	2.95	–	–	–	–	–	–	–	–	–	–
		B8	32	–	12	3	53	0.57	0.78	1.4	10.76	–	–	–	–	–	–	–	–	–	–
		B9	60	16	14	5	5	0.6	1.15	1.15	13.19	1405	0.975	43.42	2203	0.953	43.42	0.507	–	–	–
		B10	65	–	21	–	14	0.85	1.91	2.14	19.56	1403	0.948	44.21	2202	0.907	48.47	0.452	–	–	–
		B11	44	15	6	26	9	0.46	0.37	1.09	5.4	–	–	–	–	–	–	–	–	–	–
		B12	53	37	1	8	1	0.34	−0.12	1.22	0.62	1403	0.913	41.08	2202	0.884	50.79	0.442	–	–	–
		B13	51	24	6	2	17	0.44	1.17	1.35	5.17	1405	0.976	41.31	2203	0.914	43.5	0.446	–	–	–

[a] K-Si minerals: potassium silicate minerals (mainly: K-feldspar, muscovite and illite).

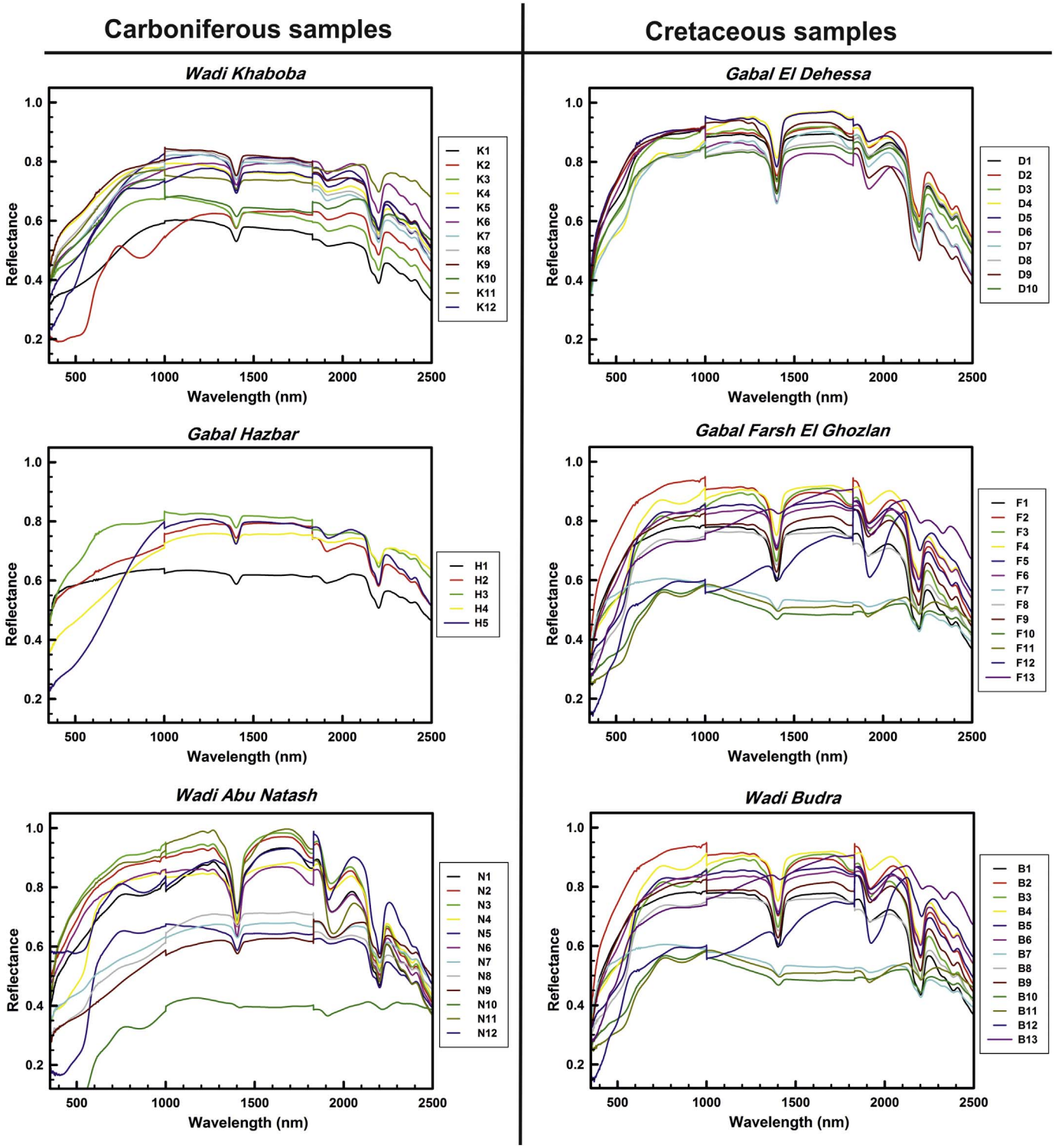

Fig. 4. Shortwave Infrared (SWIR) spectra of Carboniferous and Cretaceous Abu Zenima kaolins.

4. Results

4.1. Kaolin grade

The kaolinite content in the studied samples range from 9 to 96 wt% (Table 1). Hence, the sample grades are controlled by variable amounts of other mineral phases, mainly quartz, and lesser quantities (normally below 10%) of muscovite-illite, anatase, hematite, carbonates, sulphates and others (Awad et al., 2017a). According to Kogel et al. (2006), the kaolinitic mudrocks can be classified, based on kaolinite and/or halloysite contents and quartz and/or feldspars in the clay matrix, into kaolinitic sand-or-siltstone, sandy-or-silty kaolin and kaolin grades, with 10–50%, 50–75% and > 75% kaolinite respectively. The mean size of detrital fraction in the studied samples does not exceed the silt-sized grains (10 μm), as indicated by petrographic observations. Therefore, 48% of the studied samples are considered as kaolin grade, 40% of the samples are silty-kaolin and 12% are kaolinitic siltstone.

Finally, if we take into account the iron content variabilities, and

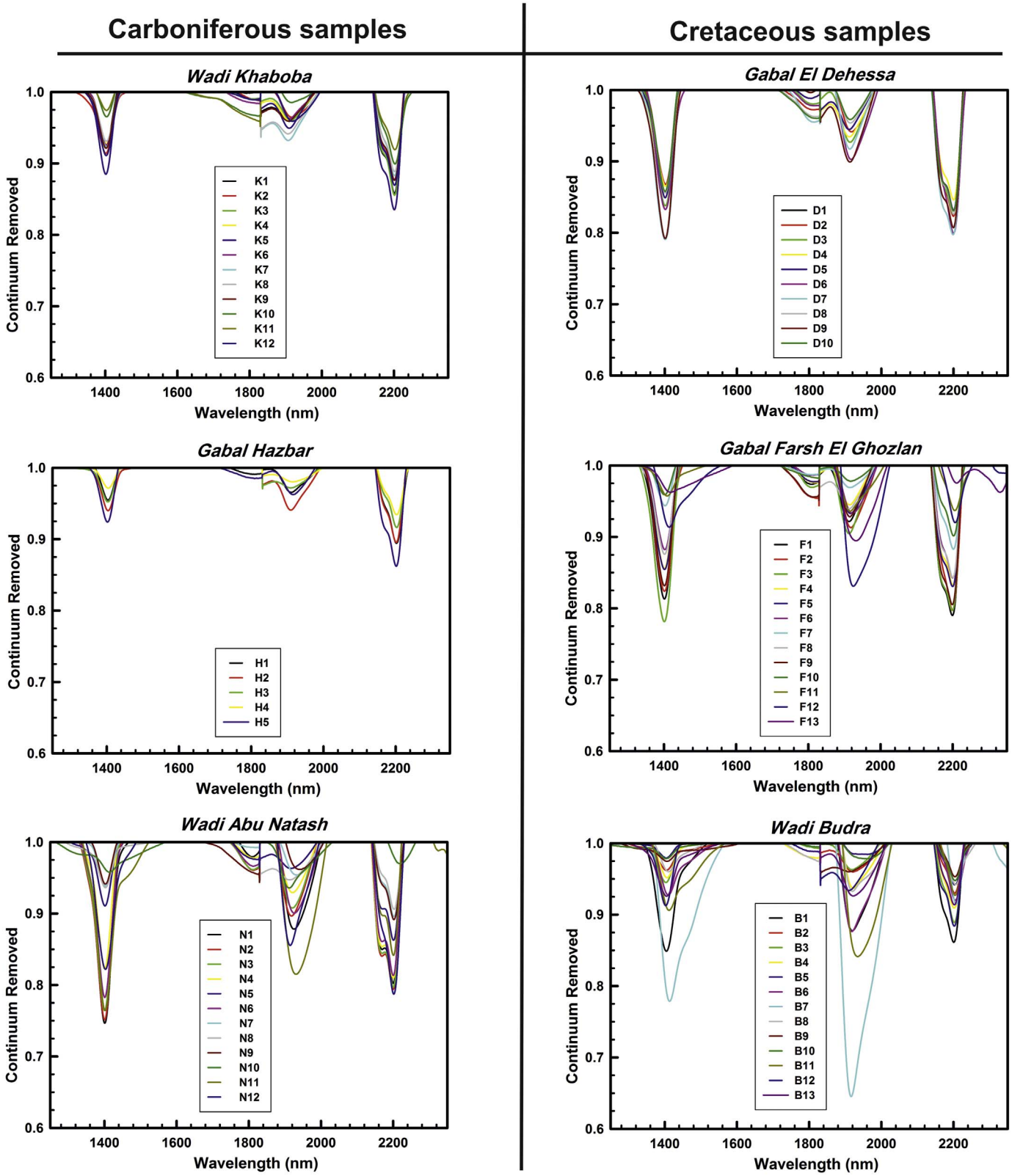

Fig. 5. Continuum removed spectra of Carboniferous and Cretaceous Abu Zenima kaolins.

according to Herron's (1988) model, the Abu Zenima samples can be classified into two different types of kaolin deposits: ferrugineous (Log [Fe_2O_3/K_2O] > 0.6, most of the Cretaceous samples) as they contain Fe-oxides and titanium minerals contents > 3%, and non-ferrugineous (Log[Fe_2O_3/K_2O] < 0.6, most of the Carboniferous samples), as they do not exceeded 3% Fe-Ti oxide mineral contents.

4.2. Kaolinite structural order-disorder

The structural order of kaolinite in the studied kaolin grade deposits (> 75% kaolinite) varied widely. The Hinckley Index (HI) ranges from 0.27 to 1.50, the Stoch Index (IK) ranges from 0.54 to 1.5 and the Liétard Index (R2) ranges from 0.48 to 1.20. The larger the value of the

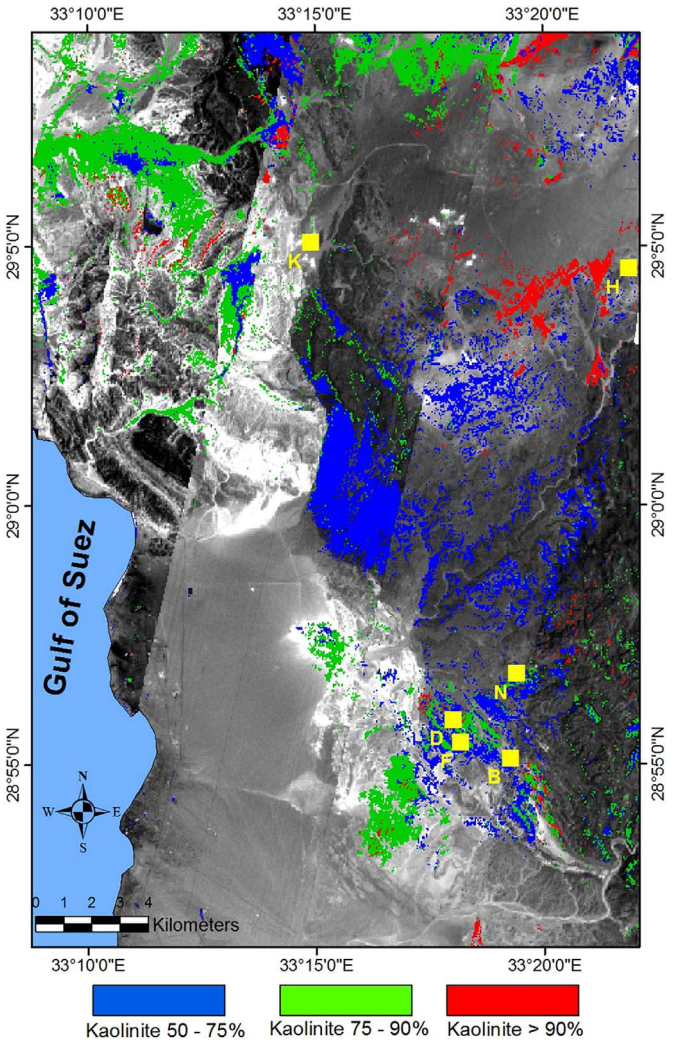

Fig. 6. Spectral Angel Mapper (SAM) classification of Hyperion for discrimination of Abu Zenima kaolin quality based on kaolinite richness (area inside dashed borders in Fig. 1).

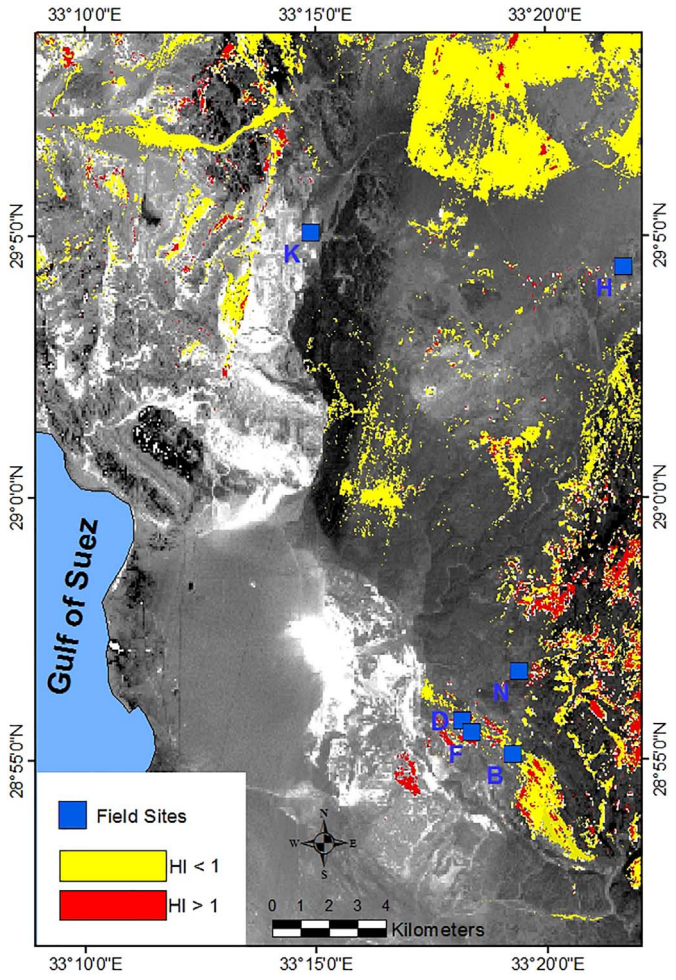

Fig. 7. Spectral Angel Mapper (SAM) classification of Hyperion for identification of Abu Zenima kaolinite order-disorder based on Hinckley Index (HI) (area inside dashed borders in Fig. 1).

HI and R2 indices, the greater the structural order, while the larger the value of the IK, the greater the disorder. Carboniferous kaolinite (samples N, K and H) exhibits high structural order (HI and R2 > 1; IK < 1), while most of the Cretaceous kaolinite (samples B, D and F) have structural disorder (HI and R2 < 1; IK mainly > 1, Table 1). It is observed that there are strong positive correlations ($R^2 = 0.96$) when Hinckley Index (HI) and Liétard index (R2) are compared, and strong negative correlation ($R^2 = 0.90$) to Hinckley Index (HI) against Stoch Index (IK), while the R2 versus IK illustrated relatively lower negative correlation (R2 = 0.89). Hence, the Hinckley index measurements showed high accuracy with quartz contents < 20%, titaniferous minerals content is < 5% and the other phyllosilicates and K-feldspar contents is < 4% (Table 1).

4.3. Spectral features and parameters

Kaolinite spectral analysis shows that the prominent absorption features occur around ~1400, ~1900, ~2200 and 2300 nm (Fig. 4). The wavelength regions from 1400 to 2450 nm have been assigned to the first harmonic of inner-surface (OH) stretching fundamentals vibration modes, the combination of outer-surface (OH) stretching overtone and Al—OH bending (Brindley et al., 1986; Johnston et al., 1998). The position, depth, and full-width-half-maximum (FWHM) of the cited absorption features were calculated for all of the continuum-removed spectra measured in samples with kaolinite content > 50%, that are defined as silty-kaolin and kaolin grades (Table 1 and Fig. 5). The 22SP-Index was calculated only for the kaolin grade samples (i.e. kaolinite > 75%, Table 1). The results indicated that there are shifting and changes in the morphology of the absorption features around the regions 1400 and 2200 nm, as well as the calculated 22SP-Index with changes of the kaolinite contents (%) and the structural order indices HI, IK and R2.

4.4. Image classifications

Spectral Angle Mapper (SAM) supervised classifications was used to identify kaolin distribution on the Hyperion images using the measured spectra of samples with different crystallinity and quality. Results show that the kaolin zones with high kaolinite richness (> 90%) are concentrated in the northeast part of the study area around field site "H" (Fig. 6, identified by red color pixels). There are also few red pixels distributed in the northwestern and southern parts of the study area. Kaolin grade with kaolinite contents 75–90% were identified by green color pixels and concentrated along the north western side of the study area and around field sites B, D, and F. There are also few green pixels distributed over the southeastern part of the study area. The low grade kaolin outcrops with kaolinite contents 50–75% are identified with blue color and concentrated in the central part of the study area. There are also some blue pixels distributed around sites N, D, F, and B.

Kaolinite order-disorder degrees were also identified using SAM supervised classification. Fig. 7 shows the distribrution of very high

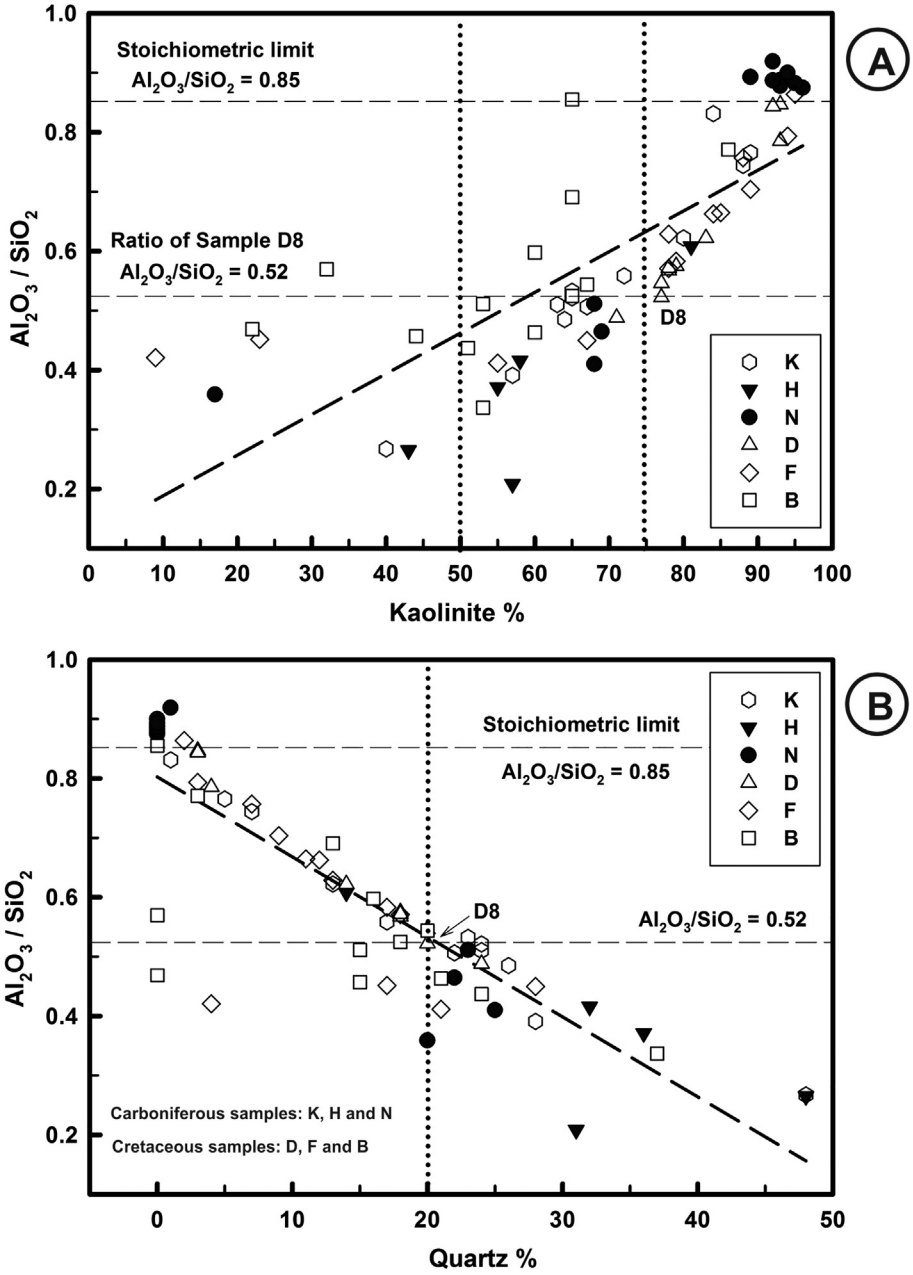

Fig. 8. Abu Zenima kaolin grades and quality classified based on the ratio Al_2O_3/SiO_2 versus kaolinite (A) and quartz (B) as main impurity, contents.

ordered kaolinites (HI > 1, red piexels) and disordered (HI < 1, yellow pixels) kaolinites, which includes lower ordered to disordered kaolinites. Red pixels close to the D, F, and B outcrops correspond to Carboniferous outcrops belonging to the Abu Thora Formation, in concordance with the geological map (Fig. 1).

5. Discussion

It is almost impossible to find kaolin deposits with pure kaolinite, given that lesser amounts of accompanying minerals are normally present. A 100% pure kaolin must exhibit around 46.5% SiO_2, 39.5% Al_2O_3 and 14% H_2O, and hence highest SiO_2 values are normally associated with quartz, K_2O and Na_2O to mica and/or feldspars, MgO and CaO to smectite, but remarkable CaO and/or MgO contents to carbonate minerals (calcite, dolomite), TiO_2 to anatase or rutile, Fe_2O_3 to iron oxi-hydroxides minerals (and rarely to ferric iron substituted for aluminum in kaolinite), and considerable Cl^- or SO_3^{--} to halite or gypsum, respectively. Trace amounts of Ni, Cr, V and Nb in raw kaolin deposit are mainly due to substitution for Ti in anatase (Wilson, 1961; Schroeder et al., 2004; Kogel et al., 2006). The selection of the beneficiation method for upgrading and improvement of crude kaolinitic rocks depend mainly on the abundance of kaolin minerals, as well as concentrations, grain or particle size distributions and densities of the detrital clastic impurities (e.g. quartz, feldspar, anatase, etc) and concentrations of the iron oxi-hydroxides minerals (e.g. hematite, goethite, etc).

The kaolin quality was discriminated by plotting kaolinite and quartz concentrations versus the Al_2O_3/SiO_2 ratios (Fig. 8). All the kaolin samples with > 75% kaolinite exhibited Al_2O_3/SiO_2 values ranged from the minimal limit 0.52 (at kaolin sample D8 with 77% kaolinite, 20% quartz and free of other silicate phases) and increased normally up to the stoichiometric limit (Al_2O_3/SiO_2 = 0.85) of kaolinite. The lower grades silty-kaolin and kaolinitic siltstone samples (kaolinite < 75% and < 50%, respectively) exhibited Al_2O_3/SiO_2 ratio

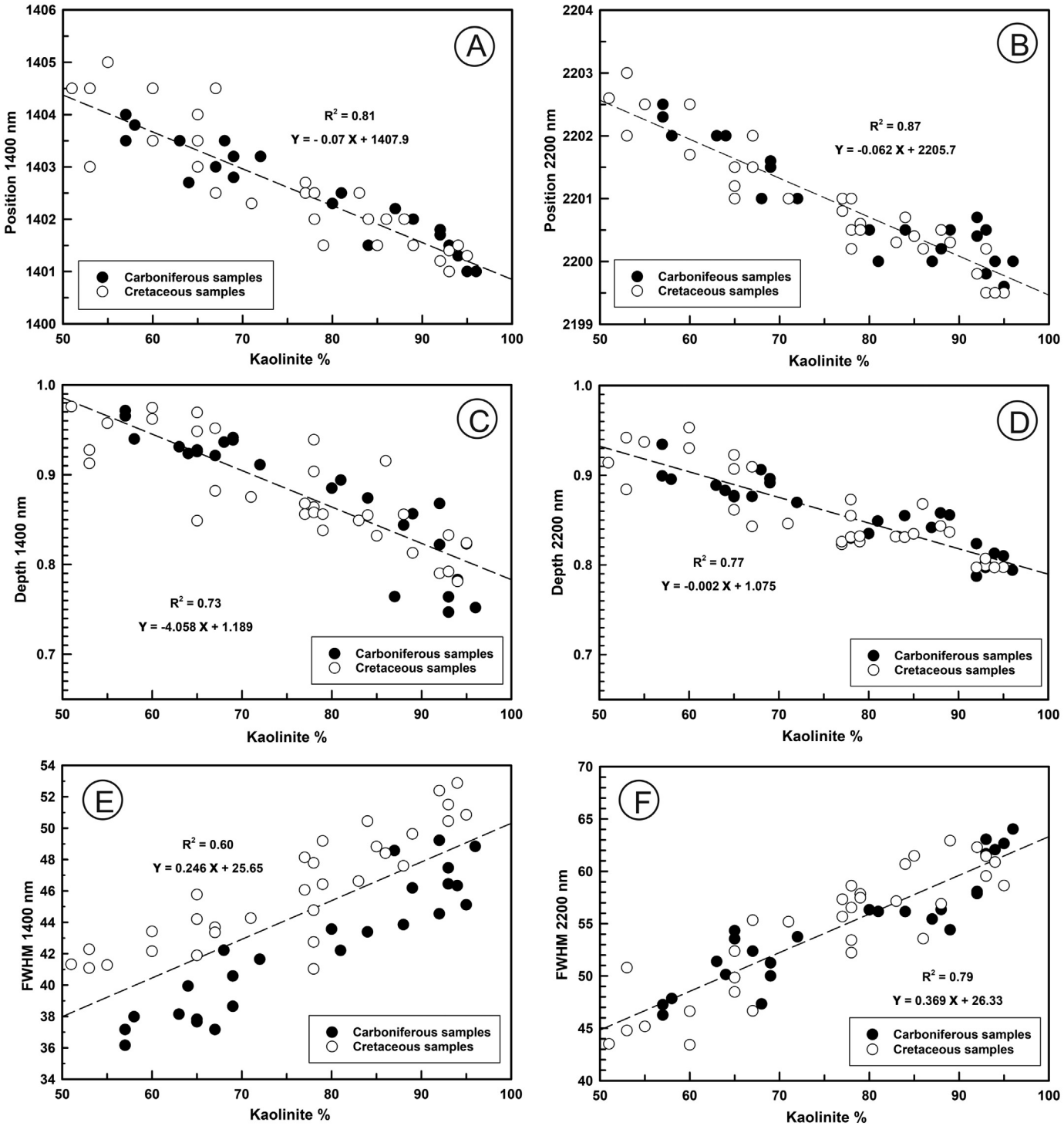

Fig. 9. Position, depth and FWHM of absorption features attributes of 1400 and 2200 nm spectral peaks versus kaolinite content (> 50% grades).

mainly < 0.52 (except some B samples) and these are influenced significantly by quartz, mica and carbonate contents.

Aparicio and Galán (1999) studied the interference and sensitivity of all the kaolinite structural order indices (i.e., HI, QF, IK, R2, FWHM and others) in relation to the kaolin mineralogical composition as well as their mutual empirical relationships. They interestingly concluded that all of these indices cannot be measured with kaolinite contents < 20 wt% as their precision increases with the high kaolin grades. The precision of the HI and QF measurements are highly influenced by any impurities, while the R2, FWHM and IK exhibit higher accuracy as they are not influenced by the associated quartz, feldspars and iron hydroxide mineral phases, but the FWHM is sensitive to chlorite and halloysite, and the IK is influenced by any phyllosilicate impurities.

The studied Carboniferous kaolin samples exhibited high kaolinite structural orders (HI and R2 > 1 and IK < 1), high Al_2O_3 and low Fe_2O_3 contents, and they can be regarded as soft kaolins (the majority of these samples are laminated and easily fractured in the field structure). Conversely, the Cretaceous samples were mostly characterized by kaolinite structural disorder, relatively low Al_2O_3 and higher Fe_2O_3 contents, so they can be considered as hard kaolins (the majority of these samples are massive and compact in the field structure).

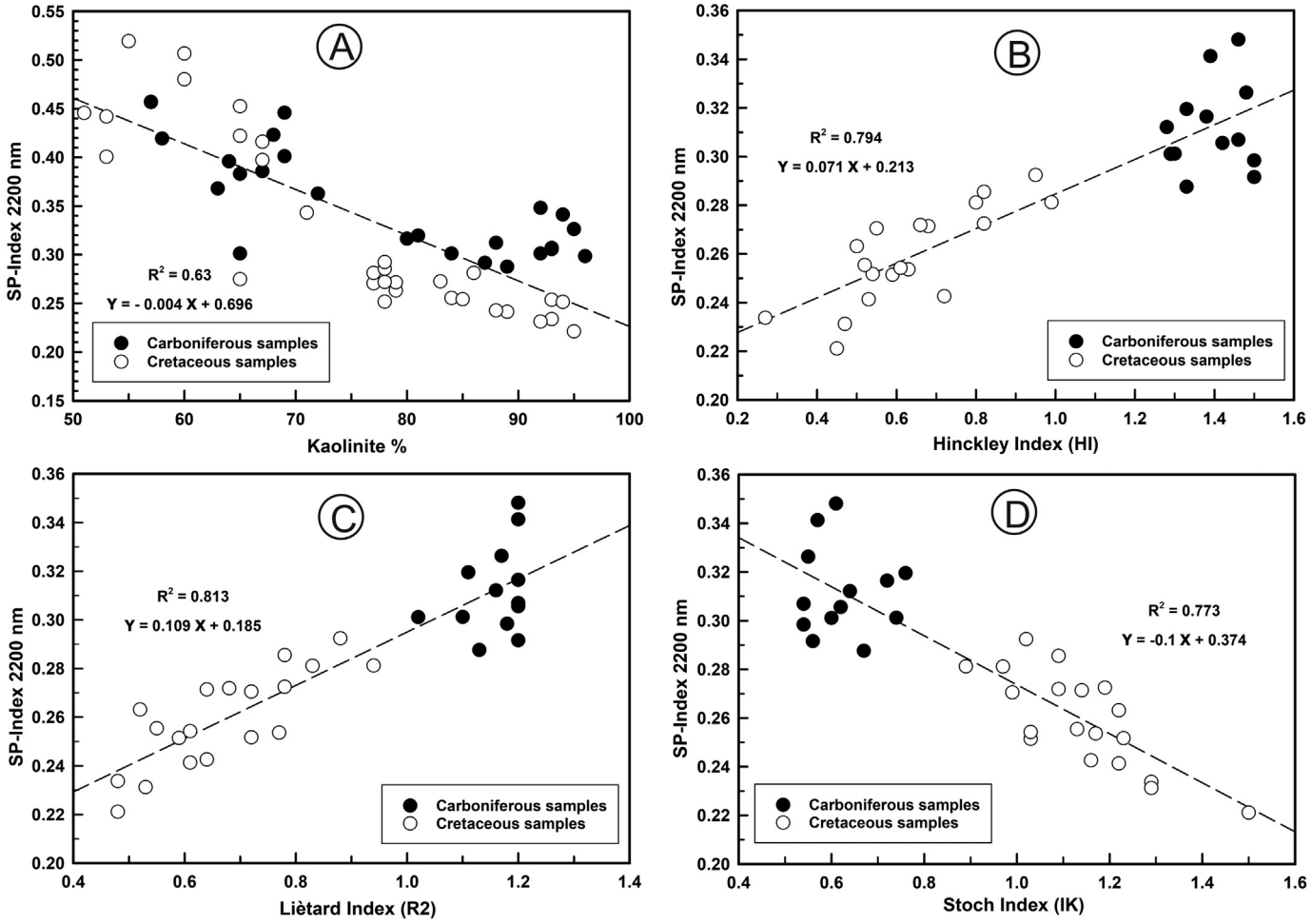

Fig. 10. Effects of kaolinite richness and structural order-disoeder degree (by HI, R2 and IK indices) on the proposed 22SP-Index (at 2200 nm).

Correlation analysis of the absorption features attributes indicated that the shifting and changes in the morphology of the absorption features around the regions 1400 and 2200 nm of the kaolinite spectra, as well as the calculated 22SP-Index, seem to be in a certain way specifically related with both the kaolinite richness (wt%) and the structural order-disorder indices (HI, R2 and IK) for the measured powdered-module samples, but not good correlations were observed for the consolidated-module samples. This could be due to the higher color homogeneity of the powdered samples when compared to the consolidated samples, which exhibit a rough surface.

Hence, in the kaolin samples with kaolinite content > 50%, the measured absorption features around 1400 nm showed negative correlations when kaolinite richness and peak position and depth are compared (R^2 = 0.81 and 0.73, Fig. 9A and C), while kaolinite richness showed positive correlation with FWHM (R^2 = 0.60, Fig. 9E). By the same way, when peak around 2200 nm is analysed, negative correlations are found between kaolinite richness and peak position and depth (R^2 = 0.87 and 0.77, Fig. 9B and D), while exhibited positive correlations (R^2 = 0.79) with FWHM (Fig. 9F). By its hand, the 22SP-Index showed negative correlations with kaolinite richness (R^2 = 0.63, Fig. 10A).

With regards to the structural order-disorder, good correlations have been found between the proposed 22SP-Index and the order-disorder indices for samples with kaolinite contents > 75%. The 22SP-Index showed positive correlations with Hinckley (HI) and Liétard (R2) indices (R^2 = 0.79 and 0.81, Fig. 10B and C) and negative correlations with the Stoch Index (IK) (R^2 = 0.77, Fig. 10D).

It could be stated, therefore, that the peak position, depth and FWHM of the spectral peaks around 1400 and 2200 nm, as well as the 22SP-Index, are related to kaolinite richness for samples with kaolinite contents > 50%, and that the 22SP-Index is also related to the structural order-disorder degree in samples with kaolinite contents > 75%. This limited extend of the 22SP-Index applicability to the cited structural order-disorder indices can be attributed to the influence of the mineral impurities on their measurements.

In over all, the obtained results indicated that spectral analysis of VNIR and SWIR and SAM classification methods could be successfully applied and they can be considered as promising for identifying and mapping kaolins with different qualities and structural order-disorder degrees.

6. Conclusions

The studied Abu Zenima kaolins are differentiated on the basis of their age, mineralogical and geochemical characteristics and structural order. The soft Carboniferous kaolins are characterized by ordered kaolinite (HI and R2 indices > 1, IK index < 1) of relatively high alumina and low iron oxide content, while the hard Cretaceous kaolins exhibited disordered kaolinite (HI and R2 < 1, IK > 1) with relatively low alumina and higher iron oxide contents. The spectral absorption features, especially those at 1400 and 2200 nm, can be considered as the most important characteristic attributes for discriminating qualities of the Abu Zenima kaolin deposits as provided good correlations with kaolinite richness for deposits containing > 50% kaolinite. The 22SP-Index only is related with the structural order-disorder degree in kaolin grade deposits (> 75% kaolinite).

Acknowledgments

This work is funded by the Egyptian Cultural Affairs and Missions Sector (Plan 2013-2014), Ministry of Higher Education, in collaboration with the Group CTS-946 (Junta de Andalucía) and Project UNGR15-CE-3531 (Ministerio de Economía y Competitividad, Spain).The first author is very grateful to Professor Emeritus: Mahmoud Hassaan El-Basha, the founder of the geochemistry school in Egypt. Deep thanks also to Dr. Arafa F. El Balkemy (Geology Dept., Al Azhar University in Cairo) and Dr. Abdel Rahman Hazem (National Authority for Remote Sensing & Space Sciences, NARSS - Egypt) for their assistance to create the geological illustrations.

References

Abd El Razek, M.M., 1994. Geology and processing trials on kaolin bearing sandstone from the gulf of Aqaba and Abu Zeneima area, Southern Sinai, Egypt. In: Proc. 1st Internat. Symp. on industrial applications of clays, Cairo, Egypt, pp. 78–88.

Abdallah, A.M., Adindani, A., Fahmy, N., 1963. Stratigraphy of Upper Paleozoic rocks, western side of the Gulf of Suez, Egypt. In: Egyptian Geological Survey, (18 pp.).

Abdel Karim, A.M., 1996. Petrogenesis of late pre-Cambrian younger granites from southwest Sinai, Egypt. J. Mineral. Petrol. Econ. Geol. 91, 185–195.

Abdel Shafy, I.A., 1967. Geology Refractory and Economic Aspects of some Egyptian Clays. PhD. Geol., Fac. Sci., Ain Shams Univ., Cairo, Egypt (163 pp.).

Amer, R., Kusky, T.M., Ghulam, A.A., 2010. Lithological mapping in the Central Eastern desert of Egypt using ASTER data. J. Afr. Earth Sci. 56, 75–82.

Amer, R., Kusky, T.M., El Mezayen, A., 2012a. Remote sensing detection of gold related alteration zones in Um Rus area, Central Eastern desert of Egypt. Adv. Space Res. 49, 121–134.

Amer, R., Sultan, M., Ripperdan, R., Encrancian, J., 2012b. Structural architecture for development of mrginal extensional subbasins in the Red Sea active rift zone. IJG 3, 133–152.

Amer, R., Al Mezayen, A., Hasanien, M., 2015. ASTER spectral analysis for alteration minerals associated with gold mineralization. Ore Geol. Rev. 75, 239–251.

Amigo, J.M., Bastida, J., García Agramut, M.J., Sanz, M., Galván, J., 1994. Crystallinity of Lower Cretaceous kaolinites of Teruel (Spain). Appl. Clay Sci. 9, 51–69.

Aparicio, P., Galán, E., 1999. Mineralogical interference on kaolinite crystallinity index measurements. Clay Clay Miner. 47, 12–27.

Awad, M.E., López-Galindo, A., El-Rahmany, M.M., El-Desoky, H.M., Viseras, C., 2017a. Characterization of Egyptian kaolins for health-care uses. Appl. Clay Sci. 135, 176–189.

Awad, M.E., López-Galindo, A., Setti, M., El-Rahmany, M.M., Viseras, C., 2017b. Kaolinite in pharmaceutics and biomedicine. Int. J. Pharm. 533, 34–48.

Baioumy, H.M., 2014a. Provenance of sedimentary kaolin deposits in Egypt: evidences from the Pb, Sr and Nd isotopes. J. Afr. Earth Sci. 100, 532–540.

Baioumy, H.M., 2014b. Mineralogy and geochemistry of clay fractions from different saprolites, Egypt: implications for the source of sedimentary kaolin deposits. Russ. Geol. Geophys. 55, 1367–1378.

Baioumy, H.M., Gilg, H.A., Taubald, H., 2012. Mineralogy and geochemistry of the sedimentary kaolin deposits from Sinai, Egypt: implications for control by the source rocks. Clay Clay Miner. 60 (6), 633–654.

Barry, 2001. P.EO-1/Hyperion Science Data User's Guide. TRW Space, Defense & Informations Systems, Redondo Beach, CA.

Boardman, J.W., Kruse, F.A., 1994. Automated spectral analysis: A geologic example using AVIRIS data, north Grapevine Mountains, Nevada. In: Proceedings, Tenth Thematic Conference on Geologic Remote Sensing. Environmental Research Institute of Michigan, Ann Arbor, MI, pp. 407–418.

Brindley, G.W., Chih-Chun, K., Harrison, J.L., Lipsiscas, M., Raythatha, R., 1986. Relation between the structural disorder and other characteristics of kaolinites and dickites. Clay Clay Miner. 34, 233–249.

Cabrera, J.G., Eddleston, M., 1983. Kinetics of dehydroxylation and evaluation of the crystallinity of kaolinite. Thermochim. Acta 70, 237–247.

Carretero, M.I., Gomes, C., Tateo, F., 2013. Clays, drugs and human health. In: Bergaya, F., Lagaly, G. (Eds.), Handbook of Clay Science, Second edition. Part B. Techniques and Applications Elsevier, Netherlands, pp. 711–764 (Chapter 5.5).

Ciullo, P.A., 1996. Industrial minerals and their uses: A handbook and formulary. By Noyes Publication, USA (632 pp.).

Clark, R.N., Roush, T.L., 1984. Reflectance spectroscopy: quantitative analysis techniques for remote sensing applications. J. Geophys. Res. 89 (7), 6329–6340.

Clark, R.N., King, T.V.V., Klejwa, M., Swayze, G.A., 1990. High spectral resolution spectroscopy of minerals. J. Geophys. Res. 95, 12653–12680.

Conoco, 1987. Geologic map of Egypt. Egyptian general authority for petroleum (UNESCO joint map project), 20 Sheets, Scale 1:500 000. Cairo.

Datt, B., McVicar, T.R., Van Niel, T.G., Jupp, D.L.B., Pearlman, J.S., 2003. Preprocessing EO-1 Hyperion hyperspectral data to support the application of agricultural indexes. IEEE Trans. Geosci. Remote Sens. 41 (6), 1246–1259.

Ekosse, G.I.E., 2010. Kaolin deposits and occurrences in Africa: geology, mineralogy and utilization. Appl. Clay Sci. 50, 212–236.

El Aref, M.M., Abd El Wahid, M., Kabesh, M., 1988. On the geology of the basement rocks, east of Abu Zenima, west central Sinai, Egypt. Egypt. J. Geol. 32 (1–2), 1–25.

Farifteh, J., Nieuwenhuis, W., Melendez, E.G., 2013. Mapping spatial variations of iron oxide by product minerals from EO-1 Hyperion. Int. J. Remote Sens. 34, 682–699.

Fialips, C.I., Petit, S., Decarreau, A., 2000. Influence of synthesis pH on kaolinite "crystallinity" and surface properties. Clay Clay Miner. 48 (2), 173–184.

Gaffey, S.J., 1986. Spectral reflectance of carbonate minerals in the visible and near infrared (0.35–2.55 μm): calcite, aragonite, and dolomite. Am. Mineral. 71, 151–162.

Goetz, A.F.H., 1992. Principles of narrow band spectrometry in the visible and IR: instruments and data analysis. In: Toselli, F., Bodechtel, J. (Eds.), Imaging Spectroscopy: Fundamentals and Prospective Applications. Kluwer, Dordrecht, pp. 21–32.

Goetz, A.F.H., Strivastava, V., 1985. Mineralogical mapping in the Cuprite mining district. In: Proceedings of the Airborne Imaging Spectrometer (AIS) Data Analysis Workshop. vol. 85. JPL, pp. 22–29.

Gupta, V., Hampton, M.A., Stokes, J.R., Nguyen, A.V., Miller, J.D., 2011. Particle interactions in kaolinite suspensions and corresponding aggregate structures. J. Colloid Interface Sci. 359, 95–103.

Hauff, P.L., 1991. Illite crystallinity: case histories using X-ray diffraction and reflectance spectroscopy to define ore host environments. In: Proceedings of the 8th Thematic Conference on Geologic Remote Sensing, Denver, USA, April 29–May 2 1991, 447458.

Hegab, O.A., Serry, M.A., Kora, M., 1992. Abu Shabana, M. Suitability of some kaolins from west central Sinai for use in ceramic and paper industries. In: Proc. Symp. Held Jointly Egypt Geol. Surv., Mineralog. Ceramics, Cairo, pp. 5–22.

Herron, M.M., 1988. Geochemical classification of terrigeneous sands and shales from core or log data. J. Sediment. Petrol. 58, 820–829.

Hinckley, D.N., 1963. Variability in crystallinity values among the kaolin deposits of the coastal plain of Georgia and South Carolina. In: Proc. 11th Int. Conf. Clays Clay Miner, pp. 229–235.

Hughes, J.C., Brown, G., 1979. A crystallinity index for soil kaolins and its relation to parent rock, climate and soil nature. J. Soil Sci. 30, 557–563.

Hunt, G.R., 1977. Spectral signatures of particulate minerals in the visible and near infrared. Geophysics 42, 501–513.

Hunt, G.R., Salisbury, J.W., 1970. Visible and near-infrared spectra of minerals and rocks: I. Silicates. Mod. Geol. 1, 283–300.

Hunt, G.R., Salisbury, J.W., 1971. Visible and near infrared spectra of minerals and rocks: II. Carbonates. Mod. Geol. 2, 23–30.

Jafari, R., Lewis, M.M., 2012. Arid land characterization with EO-1 Hyperion hyperspectral data. Int. J. Appl. Earth Obs. Geoinf. 19, 298–307.

Johnston, C.T., Helsen, J., Schoonheydt, R.A., Bish, D.L., Agnew, S.F., 1998. Single crystal Raman spectroscopic study of dickite. Am. Mineral. 83, 75–84.

Kamel, O.A., Soliman, F.H.A., Abdel Maaboud, M.H.M., 1997. Sinai carboniferous kaolins: their mineralogy, geochemical characteristics and suitability for ceramic industry. Egypt. J. Geol. 41 (2A), 219–238.

Kerekes, J.P., Baum, J.E., 2003. Hyperspectral imaging system modeling. LLabJ 14, 117–130.

Kogel, J.E., Trivedi, N.C., Barker, J.M., 2006. Industrial Minerals and Rocks: Commodities, Markets and Uses. Society for Mining, Metallurgy, and Exploration, Inc., USA (1548 pp.).

Kora, M., 1989. Lower Carboniferous Visean, fauna from Wadi Budra, west central Sinai, Egypt. Monatshefte. Neu. Jahr. Geol. Polaon 2, 523–538.

Kora, M., 1995. Carboniferous macrofauna from Sinai, Egypt: biostratigraphy and palaeogeography. J. Afr. Earth Sci. 20 (1), 37–51.

Kruse, A., Hauff, P.L., 1991. Identification of illite polytype zoning in disseminated gold deposits using reflectance spectroscopy and X-ray diffraction: potential for mapping with imaging spectrometry. IEEE Trans. Geosci. Remote Sens. 29 (1), 101–104.

Kruse, F.A., Lefkoff, A.B., Boardman, J.B., Heidebrecht, K.B., Shapiro, A.T., Barloon, P.J., Goetz, A.F.H., 1993. The spectral image processing system (SIPS) - interactive visualization and analysis of imaging spectrometer data. Remote Sens. Environ. 44, 145–163.

Kruse, F.A., Perry, S.L., Caballero, A., 2006. District-level mineral survey using airborne hyperspectral data, Los Menucos, Argentina. Ann. Geofisc. 49, 83–92.

Kusuma, K.N., Ramakrishnan, D., Pandalai, H.S., 2012. Spectral pathways for effective delineation of high-grade bauxites: a case study from the Savitri river basin, Maharashtra, India, using EO-1 Hyperion data. Int. J. Remote Sens. 33, 7273–7290.

LaIglesia, A., Aznar, A.J., 1996. Crystallinity variations in kaolinite induced by grinding and pressure treatments. J. Mater. Sci. 31 (17), 4671–4677.

Liétard, O., 1977. Contribution á l'étude des propiétés phisicochimiques, cristallographiques et morphologiques des kaolins. ((Ph.D. thesis). Nancy, France (345 pp.)).

Mundi Index, 2007. http://www.indexmundi.com/minerals/?product=kaolin. (Year of estimate: 2007 Source: http://minerals.usgs.gov), accessed: 2018-2-07. (Archived by WebCite® at http://www.webcitation.org/6mYu6IVSh).

Murray, H.H., 1999. Applied clay mineralogy today and tomorrow. Clay Miner. 34, 39–49.

Murray, H.H., Lyons, S.C., 1955. Correlation of paper-coating quality with degree of crystal perfection of kaolinite. Clay Clay Miner. 4, 31–40.

Murray, H.H., Lyons, S.C., 1959. Further correlations of kaolinite crystallinity with chemical and physical properties. Clay Clay Miner. 8, 11–17.

Mustard, J., Murchie, S., Pelkey, et al., 2008. Hydrated silicate minerals on Mars observed by the Mars Reconnaissance Orbiter CRISM instrument. Nature 454, 305–309.

Ndlovu, B., Farrokhpay, S., Forbes, E., Bradshaw, D., 2015. Characterization of kaolinite colloidal and flow behaviour via crystallinity measurements. Powder Technol. 269, 505–512.

Perry, S.L., 2004. Spaceborne and airborne remote sensing systems for mineral exploration-case histories using infrared spectroscopy. In: King, P.L., Ramsey, M.S., Swayze, G.A. (Eds.), Infrared Spectroscopy in Geochemistry, Exploration Geochemistry, and Remote Sensing. Mineralogic Association of Canada, London, Canada, pp. 227–240.

Plançon, A., Zacharie, C., 1990. An expert system for the structural characterization of

kaolinites. Clay Miner. 25, 249–260.
Poulet, F., Bibring, J.P., Mustard, J.F., Gendrin, A., Mangold, N., Langevin, Y., Arvidson, R.E., Gondet, B., Gomez, C., 2005. Phyllosilicates on Mars and implications for early Martian climate. Nature 438, 623–627.
Pour, B.A., Hashim, M., 2011. Spectral transformation of ASTER data and the discrimination of hydrothermal alteration minerals in a semi-arid region, SE Iran. Int. J. Phys. Sci. 6 (8), 2037–2059.
Pour, B.A., Hashim, M., 2012. The application of ASTER remote sensing data to porphyry copper and epithermal gold deposits. Ore Geol. Rev. 44, 1–9.
Ptáček, P., Opravil, T., Šoukal, F., Wasserbauer, J., Másilko, J., Baráček, J., 2013. The influence of structure order on the kinetics of dehydroxylation of kaolinite. J. Eur. Ceram. Soc. 33, 2793–2799.
Range, K.J., Weiss, A., 1969. Uber das Verhalten yon kaolinitit bei hohen Drücken. Ber Deut Keram Ges 46, 231–288.
Rashed, M.A., Amer, A.M., 1994. Geological and mineralogical studies on some West Central Sinai kaolin deposits and their industrial applications. In: Proc. 1st Internat. Symp. On Industrial Applications of Clays. Cairo, Egypt, pp. 306–314.
Rowan, L.C., Mars, J.C., 2003. Lithologic mapping in the Mountain Pass, California area using advanced space borne thermal emission and reflection radiometer (ASTER) data. Remote Sens. Environ. 84, 350–366.
Rowan, L.C., Hook, S.J., Abrams, M.J., Mars, J.C., 2003. Mapping hydrothermally altered rocks at Cuprite, Nevada, using the advanced space borne thermal emission and reflection radiometer (ASTER), a new satellite-imaging system. Econ. Geol. 98, 1019–1027.
Saied, R., 1990. The Geology of Egypt. A. A. Balkema, Rotterdam (721 pp.).
Schroeder, P.A., Pruett, R.J., Melear, N.D., 2004. Crystal-chemical changes in an oxidative weathering front in a Georgia kaolin deposit. Clay Clay Miner. 52, 211–220.
Stoch, L., 1974. Mineraly Ilaste ("Clay Minerals"). Geological Publishers, Warsaw, pp. 186–193.
Sultan, M., Arvidson, R.E., Sturchio, N.C., 1986. Mapping of serpentinites in the Eastern desert of Egypt by using landast thematic mapper data. Geology 14, 995–999.
Taib, M., 2015. The mineral industry of Egypt. Minerals Yearbook-Egypt (Advanced Release). In: U.S. Geological Survey, (13 pp.). Available at: http://minerals.usgs.gov/minerals/pubs/myb.html (web archive link, 07 February 2018), Accessed date: 7 February 2018(Archived by WebCite® at http://www.webcitation.org/6mYueyAGR).
Teh, E.J., Leong, Y.K., Liu, Y., Fourie, A.B., Fahey, M., 2009. Differences in the rheology and surface chemistry of kaolin clay slurries: the source of the variations. Chem. Eng. Sci. 64, 3817–3825.
Vasilev, N.G., Golovko, L.V., Ovcharenko, F.D., 1976. Investigation of cation-exchange capacity of kaolinite with different degrees of crystallinity. Colloid J. Russ. 38 (5), 761–766.
Vie, R., Azemaa, N., Quantin, J.C., Touraud, E., Fouletier, M., 2007. Study of suspension settling: a approach to determine suspension classification and particle interactions. Colloids Surf. A Physicochem. Eng. Asp. 298, 192–200.
Virta, R.L., 2015. Clay and shale (Advanced Release). In: 2013 Minerals Yearbook, U.S. Geological Survey, (22 pp.). Available at: http://minerals.usgs.gov/minerals/pubs/myb.html (web archive link, 07 February 2018), Accessed date: 7 February 2018(Archived by WebCite® at http://www.webcitation.org/6mYumTIZ3).
Wardhana, Y.W., Hasanah, A.N., Primandini, P., 2014. Deformation and adsorption capacity of kaolin that is influenced by temperature variation on calcinations. Int. J. Pharm. Pharmac. Sci. 6 (3), 1–2.
Wilson, M.J., 1961. Rock forming minerals: sheet silicates. Clay Miner. 3C, 13–50.
Zhang, G., Wasyliuk, K., Pan, Y., 2001. The characterization and quantitative analysis of clay minerals in the Athabasca basin, Saskatchewan: application of shortwave infrared reflectance spectroscopy. Can. Mineral. 39, 1347–1363.
Zhang, X., Pazner, M., Duke, N., 2007. Lithologic and mineral information extraction for gold exploration using ASTER data in the south Chocolate Mountains (California). ISPRS J. Photogramm. Remote 62, 271–282.